Open Access

Journal of Energy and Power Technology

LIDSEN Publishing Inc.

Original Research

Elaboration, Structural and Optical Characterization of the New Ternary Chalcogenide $SnSb_2S_5$

Assohoun Fulgence Kraidy [1], Islam M. El Radaf [2, 3], Andreas Zeinert [1], Abdelilah Lahmar [1], Aime Peláiz-Barranco [1, 4], Pardis Simon [5], Yaovi Gagou [1, *]

1. LPMC, Université de Picardie Jules Verne, 33 rue Saint Leu, 80039 Amiens cedex 01, France; E-Mails: fulgence.kraidy@gmail.com; andreas.zeinert@u-picardie.fr; lahmar2@yahoo.fr; pelaizbarranco@gmail.com; yaovi.gagou@u-picardie.fr
2. Electron Microscope and Thin Films Department, Physics Research Institute, National Research Centre, 33 El Bohoos Str., Dokki, Giza 12622, Egypt; E-Mail: elradaf11b@gmail.com
3. Department of Physics, College of Science, Qassim University, Buraydah 51452, Saudi Arabia
4. Grupo de Materiales Ferroicos, Facultad de Física - Instituto de Ciencia y Tecnología de Materiales, Universidad de La Habana, La Habana 10400, Cuba, Angola
5. Univ. Lille, CNRS, Centrale Lille, ENSCL, Univ. Artois, UMR 8181−UCCS Unité de Catalyse et Chimie du Solide, F-59000 Lille, France; E-Mail: pardis.simon@univ-lille.fr

* **Correspondence:** Yaovi Gagou; E-Mail: yaovi.gagou@u-picardie.fr

Academic Editor: Eugene S. Mananga

Special Issue: Synthesis and Characterizations of Advanced Materials for Energy Storage

Journal of Energy and Power Technology
2024, volume 6, issue 3
doi:10.21926/jept.2403013

Received: March 29, 2024
Accepted: July 04, 2024
Published: July 17, 2024

Abstract

In this study, tin antimony sulfide ($SnSb_2S_5$) thin films with 200 nm, 312 nm, and 431 nm thicknesses were successfully fabricated using thermal evaporation. These films' structural, optical, and photoanode properties were meticulously characterized to assess their suitability for photovoltaic applications. X-ray diffraction (XRD) analysis confirmed the presence of an orthorhombic symmetry phase within the *Pnma* space group, ensuring the crystalline quality of the films. Raman spectroscopy further validated the crystal structure and provided detailed identification of the vibrational active modes specific to this pseudo-binary chalcogenide

compound. Optical characterization revealed that the $SnSb_2S_5$ thin films possess direct optical bandgap energies ranging from 1.91 to 1.99 eV, making them ideal for efficient light absorption in photovoltaic devices. The refractive index (n) displayed minimal variation within the absorption region, indicating stable optical properties. At the same time, it increased proportionally with film thickness outside the absorption region, suggesting enhanced optical behavior with thicker films. This characteristic is particularly advantageous for improving the efficiency of photoanode materials. The combination of favorable structural properties, optimal bandgap energies, and tunable optical responses positions $SnSb_2S_5$ thin films as promising candidates for advanced photovoltaic and optoelectronic applications. These findings highlight the potential of $SnSb_2S_5$ in developing high-performance photoanodes, contributing to the advancement of solar energy conversion technologies.

Keywords

Thermal evaporation; thin films; $SnSb_2S_5$; microstructural; optical bandgap; refractive index (n)

1. Introduction

Chalcogenide materials are used for many applications, including nonlinear optics, optoelectronics, and photovoltaics, and intense research efforts are focused on this family of materials [1, 2]. Most reported research uses physical characterizations and compositions to optimize their performance. Structural and optical properties have been reported for materials such as $SnSb_2S_4$ [3, 4] and $Sn_2Sb_2S_5$ [5] for various applications. Various synthesis techniques have been employed to improve the physical properties of chalcogenides. These methods include vacuum evaporation, chemical bath deposition, radio frequency sputtering, immersion deposition, chemical spray pyrolysis, electrodeposition, and solid-state synthesis [6-9]. The choice of synthesis route can be adapted depending on the desired dimensions, size, stoichiometry, and morphology of the metal chalcogenides [9, 10]. Researchers in this field increasingly favor cost-effective synthesis methods, such as thermal evaporation, due to their straightforward setup and low manufacturing costs [11-13].

This study employed the thermal evaporation method to synthesize $SnSb_2S_5$ thin films on glass substrates. We characterized these films' structural and optical properties to evaluate their potential for photovoltaic applications. Optical properties were measured using UV-visible spectrophotometry, while structural and microstructural behaviors were analyzed using X-ray diffraction (XRD), scanning electron microscopy (SEM), energy-dispersive X-ray spectroscopy (EDX), and Raman spectroscopy. X-ray photoelectron spectroscopy (XPS) was also used to confirm the bandgap value and chemical composition. Our findings indicate that the synthesized $SnSb_2S_5$ films exhibit a narrow optical bandgap energy and improved crystallinity, contributing to their promising optoelectronic properties. This study investigates the optical and structural characteristics of $SnSb_2S_5$ layers to assess their suitability for incorporation into photovoltaic and optoelectronic applications.

2. Materials and Methods

The ternary chalcogenide $SnSb_2S_5$ thin films, with thicknesses of 200 nm (TAS200), 312 nm (TAS312), and 431 nm (TAS431), were successfully fabricated using the thermal evaporation method with an Edward's E306 coating unit. During the deposition process, substrates were maintained at room temperature, and the deposition rate was precisely controlled at 10 Å/sec. A molybdenum boat was used to ensure uniform film deposition, and the substrates were rotated at a consistent speed of 5 revolutions per minute. The bulk $SnSb_2S_5$ was synthesized by directly fusing high-purity elements (Sn, 99.99%; Sb, 99.99%; and S, 99.99%) in a cleaned vacuum silica tube. The furnace temperature was gradually increased at a rate of 40 K per hour until reaching 955°C, and it was maintained at this temperature for 24 hours in a sealed furnace to prevent the potential explosion hazard from sulfur vapor release. After this isothermal period, the stove was turned off, allowing the system to cool to room temperature without a specific cooling rate, as referenced in [14]. The vacuum level within the evaporation bell jar was maintained at 5×10^{-5} mbar. The film thicknesses were measured using a Bruker-Dektak-XT stylus profilometer, which enabled surface roughness measurements at the nanometer scale. Thickness measurements taken at multiple points along various lines on the film surfaces showed consistent results, with average thicknesses of 200, 312, and 431 nm for TAS200, TAS312, and TAS431, respectively. The uncertainty in these measurements was less than 2 nm.

Structural analysis was conducted using a Bruker D8 Discover X-ray diffractometer with CuKα radiation (λ = 1.5405 Å). Optical measurements were performed using a JASCO V-670 spectrophotometer over a 350-1200 nm wavelength range. To confirm the bandgap value and chemical composition, X-ray photoelectron spectroscopy (XPS) experiments were performed with a Kratos AXIS Ultra DLD spectrometer using monochromatic Al Kα radiation (1486.6 eV) at 225 W (15 mA, 15 kV). Core level and valence band spectra were collected using an analysis area of approximately 300 µm × 700 µm and a 20 eV pass energy, with an instrument base pressure of 9.31×10^{-10} mbar. The Kratos charge neutralizer system was employed for all analyses, and binding energies (BE) were corrected using the adventitious C 1 s C-C peak at 284.8 eV as a reference. The O 1 s, Sn 3d, Sb 3d, S 2 s, and VB spectra were analyzed using Casa XPS software (version 2.3.25 rev1.0Y) [14, 15], with spectra decomposition and quantification performed after Shirley-type background subtraction.

The vibrational modes were determined using a Renishaw in Via micro-Raman spectrometer with a non-polarized laser (λ = 532 nm) at spot exposition of 15 s and accumulation by 9 times. Scanning electron microscopy (SEM) images were recorded using a Quanta 200 FEI microscope (15 kV) equipped with an energy-dispersive X-ray (EDX) system to have information on the chemical composition of the studied material.

3. Results

3.1 Microstructural Properties of $SnSb_2S_5$ Thin Films

Figure 1 presents the SEM images of the sample surfaces, highlighting the topography and corresponding EDX analysis for TAS200 in Figures 1 (a, d), for TAS315 in Figures 1 (b, e), and for TAS431 in Figures 1 (c, f). In TAS200, two distinct zones were observed: large compact grains dotted by smaller particles and abundant holes. TAS315 presents a compact microstructure with 3D reliefs

in some areas. In contrast, TAS431 exhibited a different morphology, with a regular distribution of grain sprinkled with holes organized regularly through broader and more abundant compact grains. We used Image J software to determine the average crystallite sizes: TAS200: 39 nm, TAS315: 45 nm, and TAS431: 41 nm. This value seems to be larger. The EDX analysis of TAS431 revealed a significant sulfur content (26.49%) and a lower antimony content (35.14%) than TAS200 and TAS315. This observation aligns with the findings of Watanabe *et al.* [16], who reported a decrease in Sb-S bonds and an increase in Sb-Sb bonds in binary chalcogenides when the antimony with the film thickness and the content falls below the stoichiometric value of 40%. Additionally, as the tin content increases to 60%, Sb-Sb bonds rapidly decrease. Furthermore, with increased sulfur content, both Sb-Sb and Sn-Sn bonds tend to disappear, favoring the formation of new Sb-S and Sn-S bonds, consistent with previous results [16]. The presence of other elements (Na, C, O) can be attributed to the substrate.

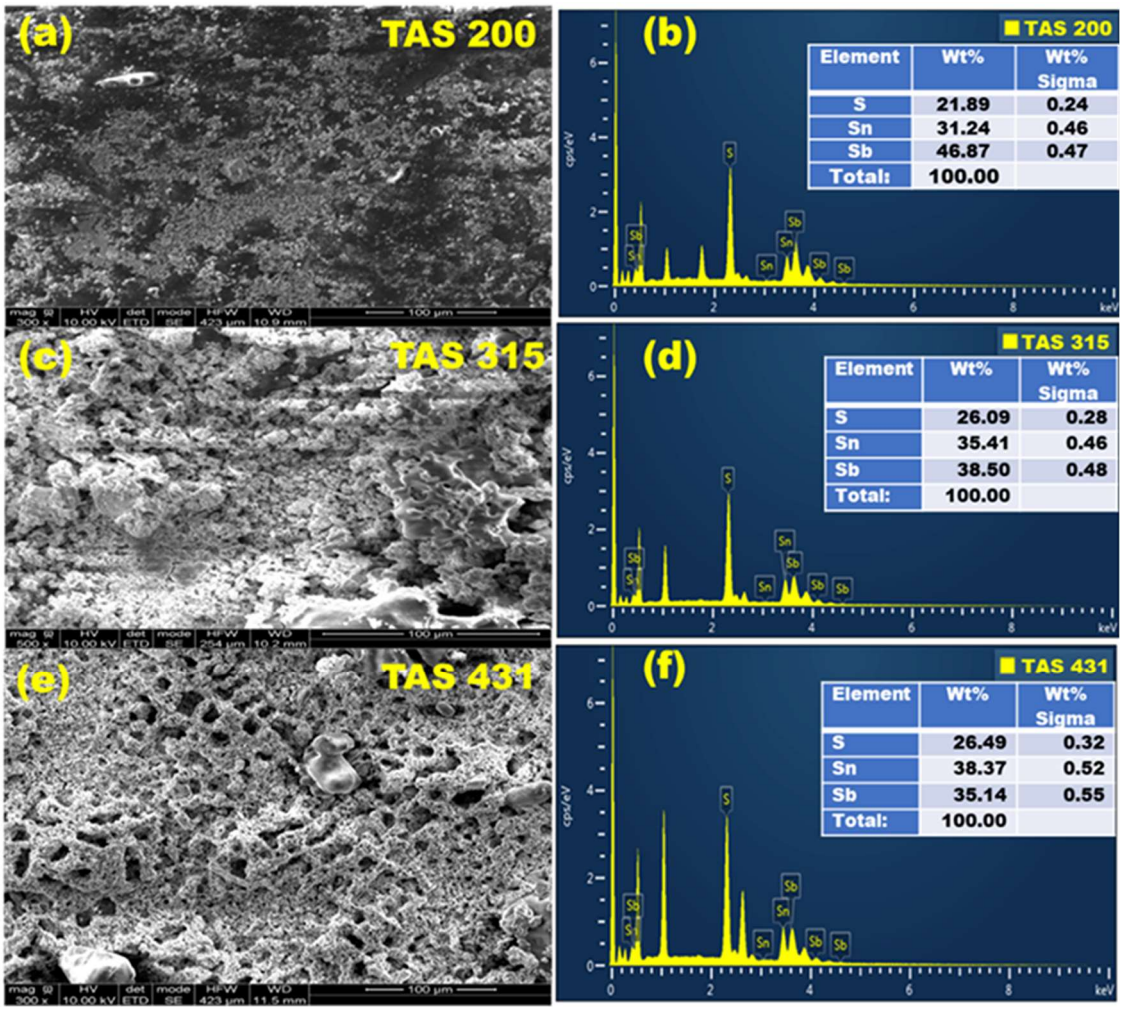

Figure 1 SEM images (a-c-e) and EDX analysis (b-d-f) for $SnSb_2S_5$ thin films: TAS200 (a-b), TAS315 (c-d) and TAS431 (e-f).

3.2 X-ray Diffraction Analysis

Figure 2 shows the X-ray diffraction pattern at room temperature for $SnSb_2S_5$ films deposited on a glass substrate. X-ray peaks were indexed accordantly to the polycrystalline orthorhombic phase

of SnS (*mp-2231)* and Sb_2S_3 (*mp-2809*) symmetries (Materials Project database), refined by using the *Pnma* space group [17, 18].

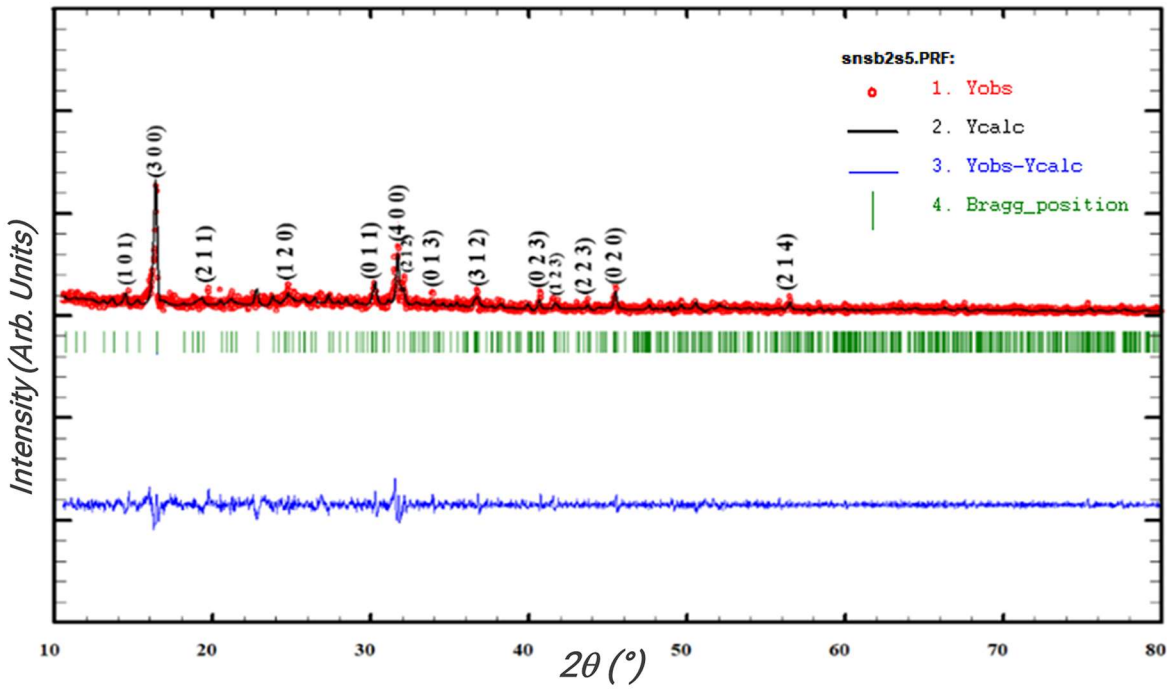

Figure 2 XRD pattern of $SnSb_2S_5$ thin film deposited on glass.

The profiles of the peaks were adjusted by using a "modified 2 Lorentzian" mathematical function, which was implemented in *FullProf* software [19], considering the asymmetric experimental peaks and the noisy data. The "Profile Matching mode with constant scale factor" refinement led to rapid convergence and satisfactory reliability factors. The refinement lattice parameters a = 15.5500 Å, b = 11.5650 Å, and c = 9.7603 Å were obtained by the *Pnma* space group with the reliability factors of χ^2 = 2.15, R_F = 4.98, R_{WP} = 13.30. The experimental (observed) and theoretical (calculated profiles) data are represented in Figure 2 by open circles (red color) and solid lines (black color), respectively, and also their difference in the blue color solid line. The vertical lines (green color) below the two first patterns correspond to the calculated Bragg's reflections. Using the following Debye-Scherrer formulas, we calculate the microstructural parameters: the number of crystallites per unit surface area (N_C), strain (ε_s), crystallite size (D), and dislocation density (δ) of the $SnSb_2S_5$ samples [20-22] as follows:

$$D = \frac{0.9\lambda}{\beta \cos\theta} \quad (1)$$

$$N_C = \frac{t}{D^3} \quad (2)$$

$$\delta = \frac{1}{D^2} \quad (3)$$

$$\varepsilon = \frac{\beta \cot\theta}{4} \quad (4)$$

where λ is the wavelength, β is the full width at half maximum (FWHM) in radian, and ϑ the diffraction angle.

Table 1 provides the microstructural characteristics of the $SnSb_2S_5$ films. This table demonstrates that crystallite size D increased with film thickness due to large grain formation during the growth process, which increased the migration of atoms. However, the other parameters N_C, δ, and $\varepsilon_s$dropped. The strain effect in the film decreases when thickness increases, leading to thin film relaxation.

Table 1 Structural parameters of the $SnSb_2S_5$ thin film.

t (nm)	$D\ (nm)$	$N_C \times 10^{-3}\ (line/nm^3)$	$\delta \times 10^{-3}\ (nm^{-2})$	$\varepsilon \times 10^{-3}$
200	*27.41*	*9.71*	*1.33*	*1.26*
312	*30.29*	*8.12*	*1.09*	*1.14*
431	*38.21*	*7.73*	*0.684*	*0.906*

The simultaneous effect on the lattice strain and crystallite size related to the peak broadening in X-ray patterns can be described by the Williamson-Hall relation [23]:

$$\beta \cos\theta = \frac{0.94\lambda}{D} + 4\varepsilon \sin\theta\,, \tag{5}$$

where β is the full width at half maximum (FWHM). Considering (β cosθ) in the Y-axis and (4 sinθ) in the X-axis, the crystallite size (D) = kλ/(Y-intercept) with k = 0.94, and the slope gives the strain values. Generally, the width β in a diffraction peak is influenced by the change in instrumental factors, change in strains, crystallite size, and crystal defects [24, 25]. The first term on the right-hand side of the equation corresponds to the Scherrer expression, which gave the crystallite size. The second part shows the change in microstrain associated with nanoparticles on the broadened peak, known as the Stokes and Willson expression [26].

When the peak broadening shows independence over 1/D, an enhancement in 1/D values increases the strain broadening, and the size of crystallites and strain are evaluated simultaneously. This analysis is not necessary for the present study. It should be engaging in the presence of thermal effects or chemical element doping effects and structural phase change [27].

3.3 Raman Study of $SnSb_2S_5$ Thin Films

Figure 3 shows the Raman spectrum for $SnSb_2S_5$ thin film TAS431 at room temperature. The same spectrum is obtained for the three studied thin films. Several vibrational active modes were observed. The nine active modes centered at 103 cm^{-1}, 150 cm^{-1}, 183 cm^{-1}, 220 cm^{-1}, 290 cm^{-1}, 306 cm^{-1}, 314 cm^{-1}, 435 cm^{-1} and 473 cm^{-1} were active and more visible. Note that Sb-S bounding with Sb-Sb and Sb-S_3 vibration for the compound Sb_2S_3 was already observed [16, 28], attributed to the modes at 170 cm^{-1} and 290 cm^{-1}. The peak at 150 cm^{-1} was attributed to the B_{3g} mode, and the peaks at 103 cm^{-1}, 183 cm^{-1}, and 220 cm^{-1} to the A_g mode [29, 30], confirming the presence of Sn-S vibration in $SnSb_2S_5$. Then, the broad peak, located between 290 cm^{-1} and 314 cm^{-1}, could be attributed to a new formation of Sb-S bonds [30].

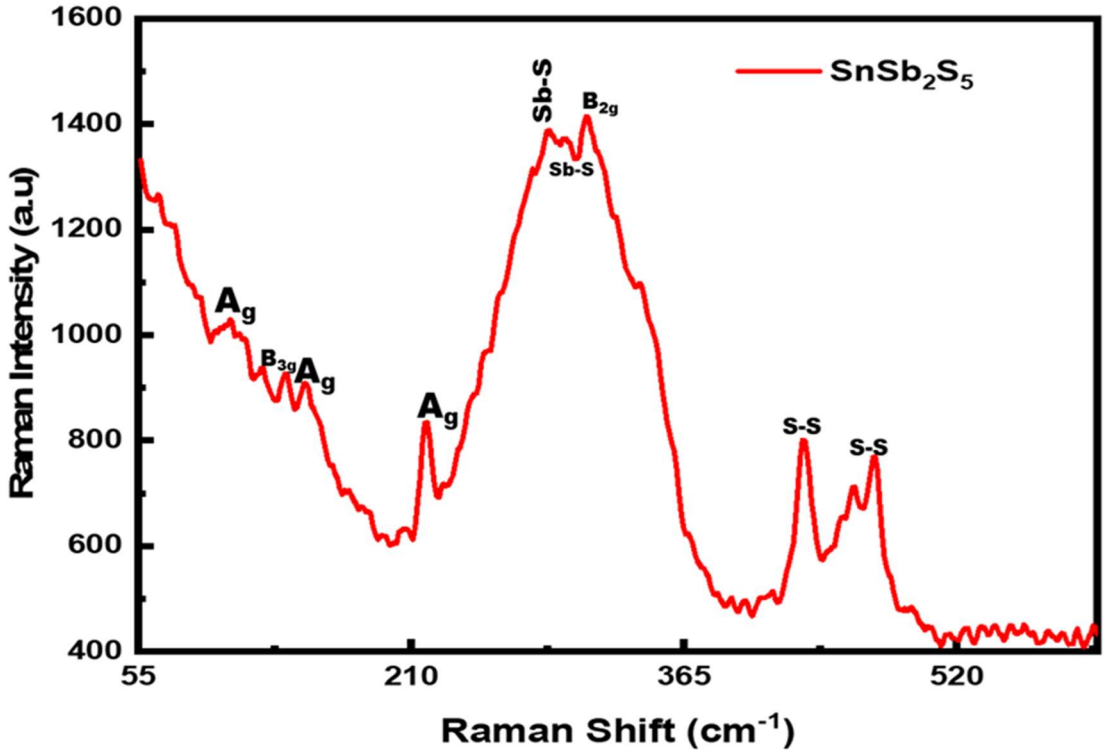

Figure 3 Raman spectrum for $SnSb_2S_5$ thin film at room temperature.

The peak at 314 cm^{-1} was attributed to the B_{2g} mode [31]. The 434 cm^{-1} and 473 cm^{-1} peaks could be attributed to the S-S bond vibrations [18, 32, 33]. From these analyses, it could be concluded that the $SnSb_2S_5$ exhibits a combination of Sb_2S_3/SnS-S vibration modes with an essential contribution of tin and sulfur.

3.4 Optical Properties of the $SnSb_2S_5$ Thin Films

The optical properties of the TAS samples were determined by analyzing the optical transmission and reflection of the materials to reveal how they interact with light. Figure 4 displays the transmittance and reflectance spectra of TAS200, TAS312 and TAS431. These TAS films have a low optical transmittance of up to 38% in visible light. It has been observed that the transmittance values decrease as the layer thickness increases from 200 to 431 nm. It was also possible to evaluate the TAS samples' reflectance value, which increases with the thickness of the films, as seen in Figure 4(b), where the reflectance value reaches almost 40%. These results corroborate the previous X-ray diffraction analysis related to the crystallization and grain size of the films.

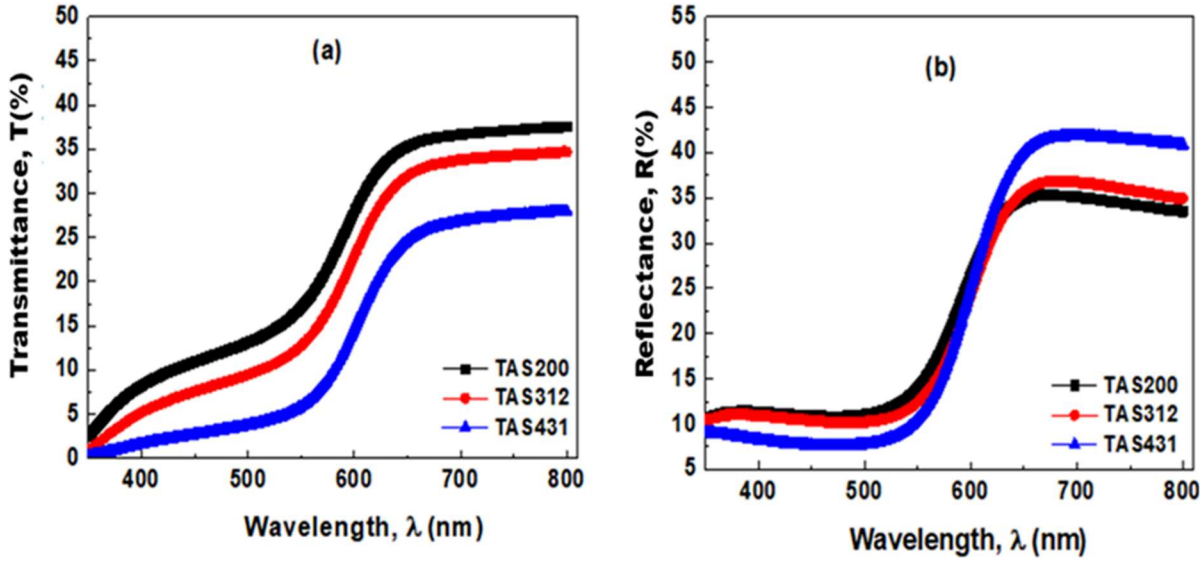

Figure 4 Transmittance and reflectance curves as a function of wavelength.

On the other side, the optical energy bandgap (E_g) of the $SnSb_2S_5$ layers was evaluated using Tauc's law [34-37]:

$$\alpha h\nu = A\left(h\nu - E_g\right)^p \tag{6}$$

where *A* is a Tauc parameter, and *p* is the type of electronic transition. In the case of the direct allowed transition, *p* = 0.5, and in the indirect allowed transition, *p* = 2.

Due to the direct electronic transition and the direct permitted transition, the energy bandgap of the TAS samples is the best fit with p = 0.5. The modification of the $(\alpha h\nu)^2$ of these TAS samples concerning photon energy is shown in Figure 5 (a). These plots were used to determine the Eg values for the TAS samples, which are 1.91, 1.95, and 1.99 eV for the TAS200, TAS312, and TSA431, respectively. According to these values, the Eg-values of thin TAS samples increase from 1.91 eV to 1.99 eV as the layer thickness increases. This trend might result from increased structural ordering and disordered or defects in localized states in the bandgap region in connection with the E_g value [21, 38, 39]. The refractive index (n) of the TAS samples was also estimated using the Kramer's-Kroning relationship [40]:

$$n = \frac{1+R}{1-R} + \left(\frac{4R}{(1-R)^2} - K^2\right)^{\frac{1}{2}} \tag{7}$$

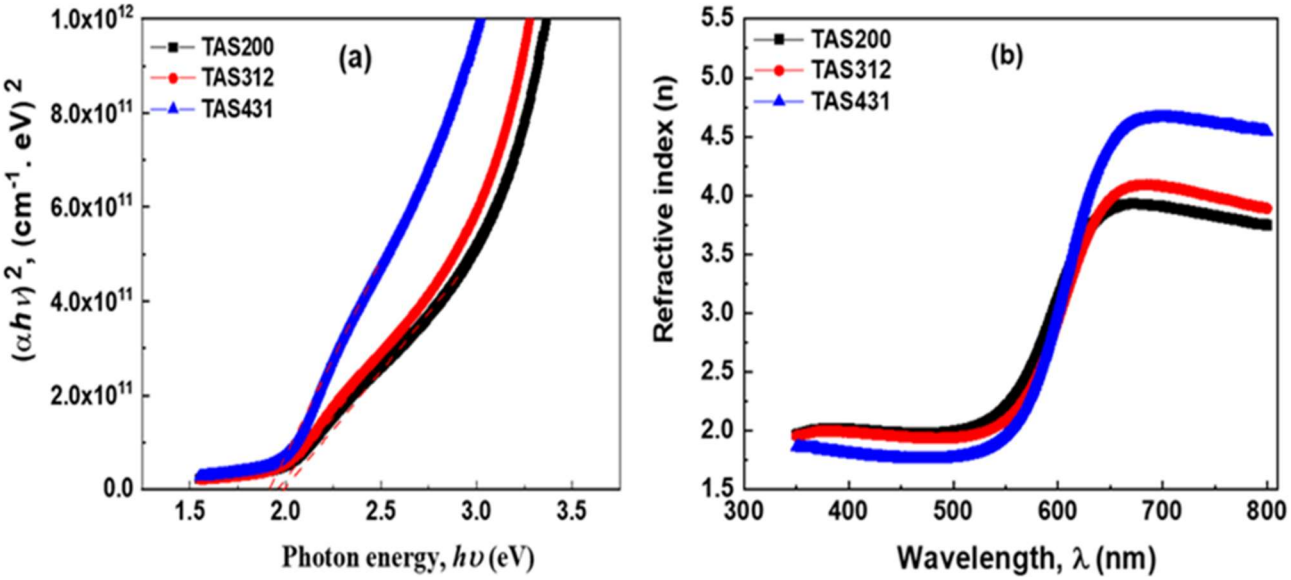

Figure 5 (a) Variation of $(\alpha hv)^2$ as a function of incident photon energy (hv) for the TAS200, TAS312, and TAS431. (b) Variation of refractive index (n) as a function of wavelength (λ) for the TAS200, TAS312, and TAS431.

Figure 5 (b) reveals the refractive index (n) plot for the TAS samples as a function of λ. This figure demonstrates that the refractive index (n) attains a peak in the absorption area and then decreases slowly towards higher wavelengths. However, the refractive index (n) increases at this area with the thickness of the sample. At 650 nm, the TAS films' refractive index (n) enlarges with increasing λ, exhibiting typical dispersive light source compatible with photoanode behavior [41].

3.5 X-ray Photoelectron Spectroscopy (XPS)

The electronic structure of the thin films was conducted using the X-ray Photoelectron Spectroscopy (XPS) technique. The chemical elements (Sb, Sn, and S) were quantified, and the valence band was studied using the same method.

3.5.1 Valence Band Analysis

Valence band XPS experiments were performed using Al Ka (1486.6) eV photon lines. Figure 6 shows the position of the valence band (EVB), which was determined using the intersection of the linear extrapolation of the leading edge of the EVB spectrum with the baseline. According to the spectrum, the value of the valence band maximum (EVB) is located at 1.66 eV below the Fermi level at 0 eV. This is expected to be inferior to the value conduction band minimum since the global bandgap is 1.91 eV for TAS200.

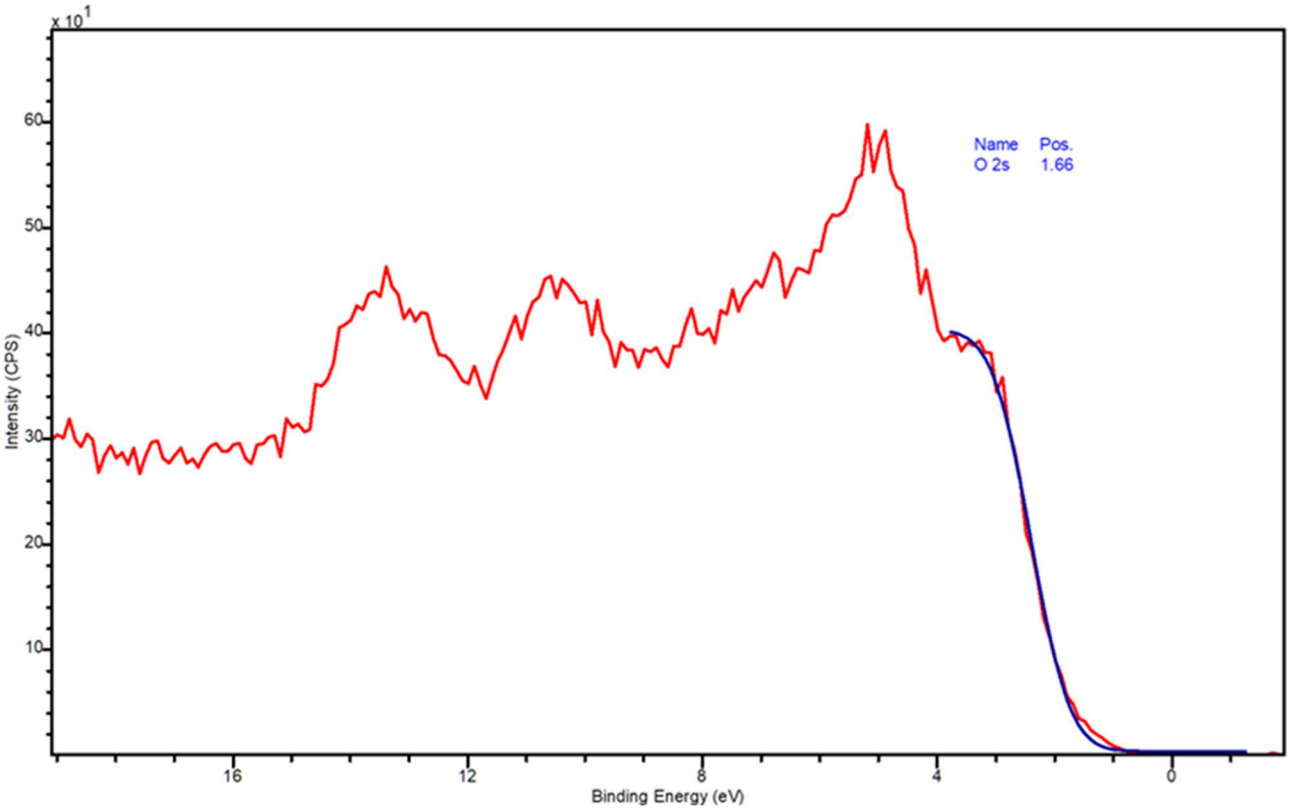

Figure 6 XPS valence band spectrum of sample TAS200 showing the maximum of the VB relative to the Fermi level.

3.5.2 Sample Chemical Composition

The XPS analysis of the $SnSb_2S_5$ material confirms the presence of the requisite chemical elements, Sn, Sb, and S.

Figure 7 shows the survey spectrum of sample TAS200. Its analysis allows us to determine the chemical species with a concentration above the detection limit at the sample's surface. The chemical elements C, O, Sn, Sb, and S are detected at the surface and Na. Traces of Ca and Cl are also found at the surface in small proportions.

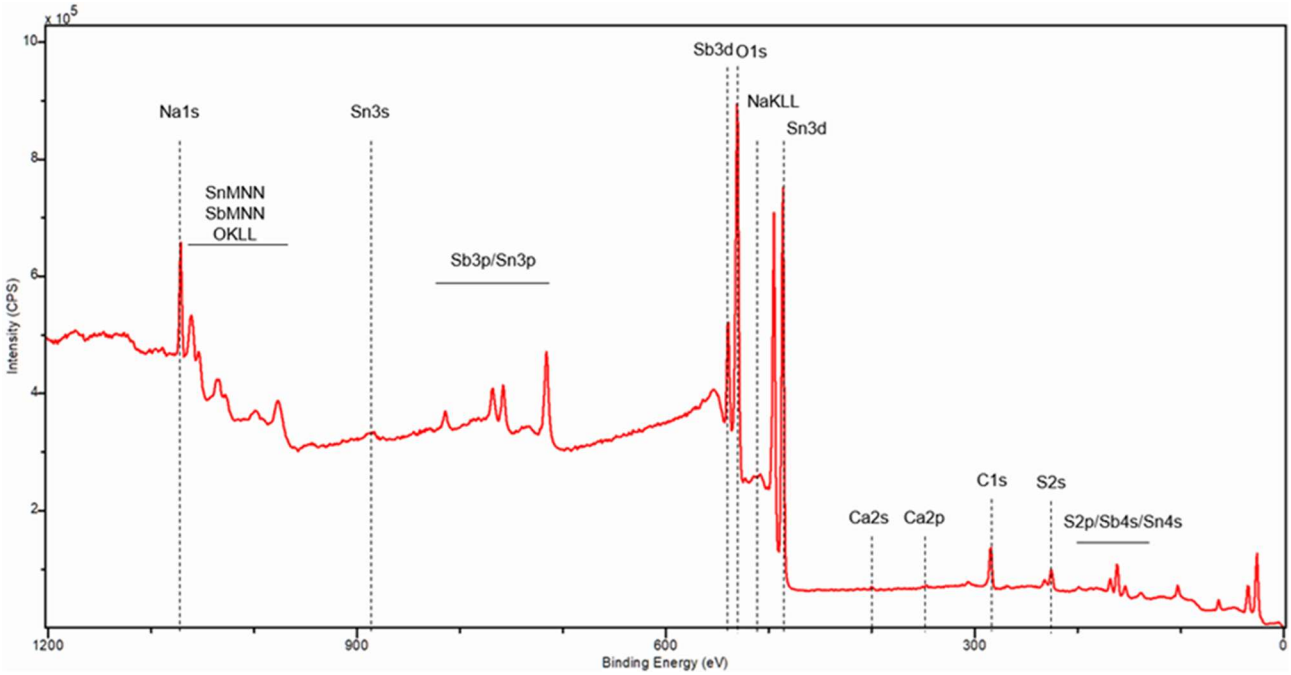

Figure 7 Global Survey spectrum recorded on TAS200 surface.

The O 1 s spectrum can be resolved into two peaks, 531.0 eV and 532.2 eV. These peaks can be attributed to lattice Sn or Sb oxide and sulfate species on the surface, respectively. Sb 3d spectrum can be resolved by two doublet peaks corresponding to Sn $3d_{5/2}$ and Sn $3d_{3/2}$ orbitals with Sb $3d_{5/2}$ contribution positioned at 529.6 and 530.8 eV and Sb $3d_{5/2-3/2}$ energy splitting of 9.3 eV. These two contributions can be attributed to Sb^{3+} and Sb^{5+} species, respectively. An additional peak is present in the O 1s - Sb 3d energy region corresponding to Na Auger electrons. Sn 3d spectrum can be resolved by a single doublet peak corresponding to Sn $3d_{5/2}$ and Sn $3d_{3/2}$ orbitals with Sn $3d_{5/2}$ BE positioned at 486.8 eV and Sn $3d_{5/2-3/2}$ energy splitting of 8.4 eV. This is characteristic of Sn^{4+} species. An additional peak is present in the Sn $3d_{3/2}$ energy region corresponding to Na Auger electrons. C 1 s spectrum is decomposed into three components attributed to adventitious carbon and localized at 284.8 (C-C, C-H bonds), 286.3 (C-OH bonds), and 288.6 eV (O-C- bonds). S 2 s spectrum was resolved with two components with BE 226.2 and 232.5 eV that can be attributed to lattice Sulfur and $(SO_4)^{2-}$ species, respectively. Figure 8 shows all decomposition investigations in the specific energy regions.

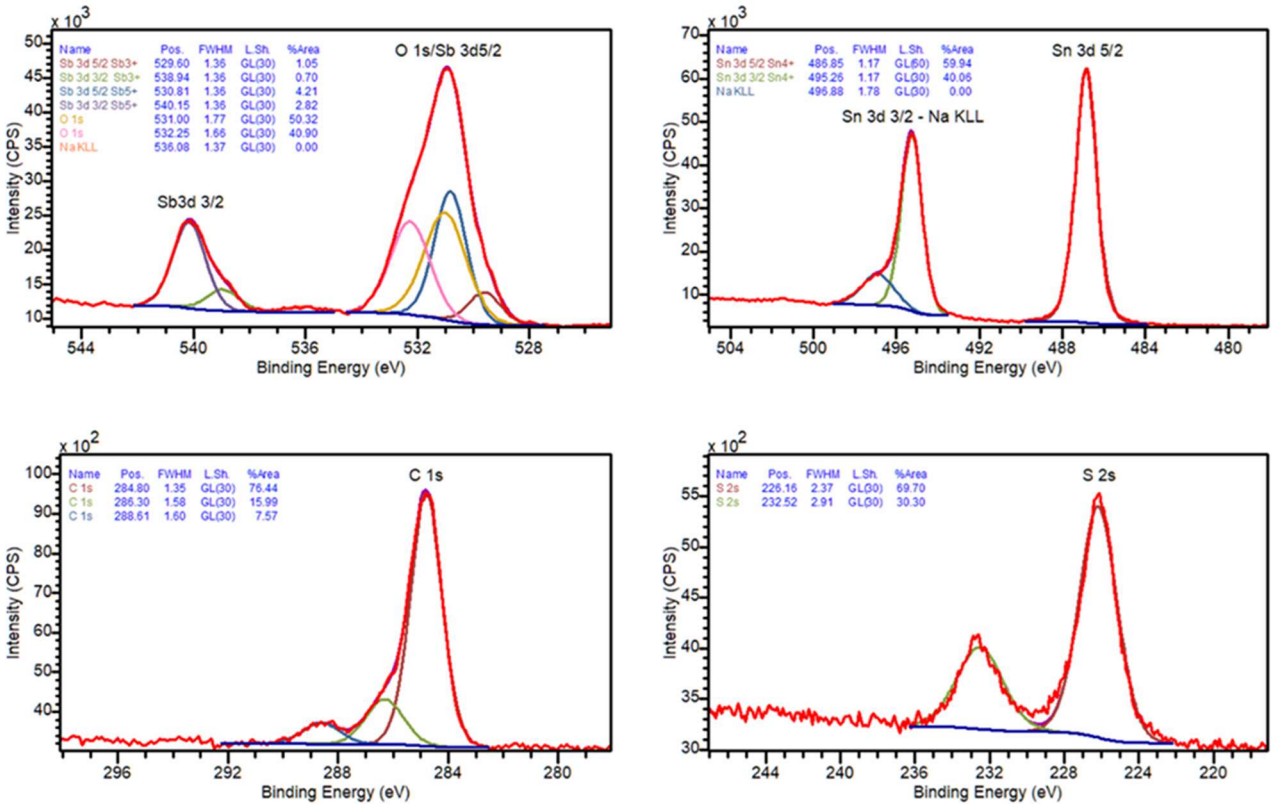

Figure 8 XPS spectra decomposed to confirm the presence of chemical elements in TAS200: (a) antimony [Sb 3d] and oxygen [O1 s], (b) Tin [Sn 3d], (c) Carbon [C 1 s], (d) Sulfur [S 2 s].

Note that it is not easy to compare EDX and XPS techniques objectively. Both techniques inform about the chemical proportions of the element in the material, but not absolute chemical composition. However, the XPS gives a more accurate proportion since it is a surface-sensitive technique that provides detailed information about the chemical states and electronic configurations of elements on the top of a few nanometers of a sample. Indeed, a table of comparison will not be strictly conclusive.

After a background removal for each spectrum, a relative atomic quantification of the chemical elements present at the surface was estimated. Determining chemical elements' nuclear masses and the Sn/Sb ratio permits accurately confirming the sample's chemical composition. Results are gathered in Table 2.

Table 2 Atomic rate in analyzed zone.

Atomic concentration (%) In analysed region	TAS200 (XPS)
Sn	14.6
Sb	5.9
S	17.7
O	61.8
Sn/Sb	2.5

4. Conclusion

Using thermal evaporation, $SnSb_2S_5$ ternary chalcogenide thin films were successfully elaborated with different thicknesses (200 nm, 312 nm, and 431 nm). Structural studies showed orthorhombic symmetry compatible with the *Pnma* space group and an average crystallite size of about 31.97 nm. The microstructural analysis showed compact films and different morphology. The optical analysis showed an energy bandgap ranging from 1.91 to 1.99 and a direct electronic transition with a refractive index (n), which decreases weakly as a function of the thickness of the films. The XPS technique confirmed the energy bandgap and chemical composition. The Fermi energy level was at 1.66 eV above the maximum valence band, and the chemical analysis revealed a Sn/Sb ratio of 2.5. In this case, surface grains are considerable and randomly distributed into the layer, inducing high absorption. Therefore, this compound can be a potential material for optoelectronic applications.

Acknowledgments

This work was supported financially by The France Ministry for Europe and Foreign Affairs (MEAE) via PHC Carlos Finlay project No 47075NF and Ministry of Higher Education and Scientific Research of Côte d'Ivoire.

Author Contributions

A. F. Kraidy: Data curation, writing-original draft preparation, investigation. I.M. El Radaf: Sample growth. A. Zeinert: Optical analysis. A. Lahmar: formal analysis. A. Peláiz-Barranco: native English contributor. P. Simon, XPS experiment and analysis. Y. Gagou, Conceptualization, Structural analysis, methodology.

Competing Interests

Authors not have any conflicts of Interest.

References

1. Suresh R, Pandiaraj M, Sankaralingam M, Giribabu K. Graphene-metal chalcogenide modified electrochemical sensors. In: Graphene-based electrochemical sensors for biomolecules. Amsterdam, Netherlands: Elsevier; 2019. pp. 139-153.
2. Zhang Y, Zhou Q, Zhu J, Yan Q, Dou SX, Sun W. Nanostructured metal chalcogenides for energy storage and electrocatalysis. Adv Funct Mater. 2017; 27: 1702317.
3. El Radaf IM. Dispersion parameters, linear and nonlinear optical analysis of the $SnSb_2S_4$ thin films. Appl Phys A. 2020; 126: 357.
4. Gassoumi A, Kanzari M. Growth and post-annealing effect on the properties of the new sulfosalt $SnSb_2S_4$ thin films. Physica E Low Dimens Syst Nanostruct. 2011; 44: 71-74.
5. Gassoumi A, Kanzari M. Optical, structural and electrical properties of the new absorber $Sn_2Sb_2S_5$ thin films. Chalcogenide Lett. 2009; 6: 163-170.
6. Kafashan H, Balak Z. Preparation and characterization of electrodeposited SnS: In thin films: Effect of in dopant. Spectrochim Acta A Mol Biomol Spectrosc. 2017; 184: 151-162.

7. Halacoglu S, Li Y, Arnold W, Shreyas V, Guo X, Jasinski JB, et al. Solvent-free and low temperature synthesis of chalcogenide Na superionic conductors for solid-state batteries. Chem Eng J. 2023; 468: 143624.
8. Chalapathi U, Poornaprakash B, Park SH. Chemically deposited cubic SnS thin films for solar cell applications. Sol Energy. 2016; 139: 238-248.
9. Hassanien AS, Sharma I, Sharma P. Optical and dispersion studies of thin $S_{35-x}Ge_{15}Sn_xTe_{50}$ films: Assessment of some physical parameters of samples. Phys Scr. 2023; 98: 045911.
10. Eisa T, Abdelkareem MA, Jadhav DA, Mohamed HO, Sayed ET, Olabi AG, et al. Critical review on the synthesis, characterization, and application of highly efficient metal chalcogenide catalysts for fuel cells. Prog Energy Combust Sci. 2023; 94: 101044.
11. Santana AL, Nair PK. Antimony sulfide selenide thin film solar cells prepared from thermal evaporation sources produced via chemical reactions. Mater Sci Semicond Process. 2023; 160: 107450.
12. Liu A, Zhu H, Zou T, Reo Y, Ryu GS, Noh YY. Evaporated nanometer chalcogenide films for scalable high-performance complementary electronics. Nat Commun. 2022; 13: 6372.
13. Almeida RM, Santos LF, Simens A, Ganjoo A, Jain H. Structural heterogeneity in chalcogenide glass films prepared by thermal evaporation. J Non Cryst Solids. 2007; 353: 2066-2068.
14. Kraidy AF, El Radaf IM, Zeinert A, Lahmar A, Peláiz-Barranco A, Gagou Y. Optoelectrical properties of the ternary chalcogenide $SnSb_2S_5$ as a new absorber layer for photovoltaic application. J Phys D Appl Phys. 2024; 57: 205102.
15. Fairley N, Fernandez V, Richard-Plouet M, Guillot-Deudon C, Walton J, Smith E, et al. Systematic and collaborative approach to problem solving using X-ray photoelectron spectroscopy. Appl Surf Sci Adv. 2021; 5: 100112.
16. Watanabe I, Noguchi S, Shimizu T. Study on local structure in amorphous Sb S films by Raman scattering. J Non Cryst Solids. 1983; 58: 35-40.
17. Raadik T, Grossberg M, Raudoja J, Traksmaa R, Krustok J. Temperature-dependent photoreflectance of SnS crystals. J Phys Chem Solids. 2013; 74: 1683-1685.
18. An C, Tang, Yang Q, Qian. Formation of crystalline stibnite bundles of rods by thermolysis of an antimony (III) diethyldithiocarbamate complex in ethylene glycol. Inorg Chem. 2003; 42: 8081-8086.
19. Rodríguez-Carvajal J. An introduction to the program. Thackeray, France: Laboratoire Léon Brillouin; 2001.
20. Holzwarth U, Gibson N. The Scherrer equation versus the 'Debye-Scherrer equation'. Nat Nanotechnol. 2011; 6: 534.
21. El Radaf IM, Hassanien AS. Effect of thickness on structural, optical, and optoelectrical properties of sprayed $CuInSnS_4$ thin films as a new absorber layer for solar cells. Physica B Condens Matter. 2023; 659: 414867.
22. Patterson AL. The Scherrer formula for X-ray particle size determination. Phys Rev. 1939; 56: 978.
23. Mote VD, Purushotham Y, Dole BN. Williamson-hall analysis in estimation of lattice strain in nanometer-sized ZnO particles. J Theor Appl Phys. 2012; 6: 6.
24. Das S, Paikaray S, Swain I, Senapati S, Naik R. Tuning in linear and nonlinear optical parameters by interfacial mixing of Sb/Ag_2Se bilayer thin films under annealing at different temperatures for optoelectronic applications. Surf Interfaces. 2023; 42: 103395.

25. Das S, Priyadarshini P, Alagarasan D, Vardhrajperumal S, Ganesan R, Naik R. Structural, morphological, and linear/non-linear optical properties tuning in $Ag_{60-x}Se_{40}Te_x$ films by thermal annealing for optoelectronics. J Non Cryst Solids. 2022; 592: 121742.
26. Priyadarshini P, Das S, Alagarasan D, Ganesan R, Varadharajaperumal S, Naik R. Observation of high nonlinearity in Bi doped $Bi_xIn_{35-x}Se_{65}$ thin films with annealing. Sci Rep. 2021; 11: 21518.
27. Abdel-Rahim MA, El-Korashy A, Hafiz MM, Mahmoud AZ. Kinetic study of non-isothermal crystallization of Bi_xSe_{100-x} chalcogenide glasses. Physica B Condens Matter. 2008; 403: 2956-2962.
28. Ota J, Roy P, Srivastava SK, Nayak BB, Saxena AK. Morphology evolution of Sb_2S_3 under hydrothermal conditions: Flowerlike structure to nanorods. Cryst Growth Des. 2008; 8: 2019-2023.
29. Chandrasekhar HR, Humphreys RG, Zwick U, Cardona M. Infrared and Raman spectra of the IV-VI compounds SnS and SnSe. Phys Rev B. 1977; 15: 2177.
30. DeAngelis AD, Kemp KC, Gaillard N, Kim KS. Antimony (III) sulfide thin films as a photoanode material in photocatalytic water splitting. ACS Appl Mater Interfaces. 2016; 8: 8445-8451.
31. Sorb YA, Rajaji V, Malavi PS, Subbarao U, Halappa P, Peter SC, et al. Pressure-induced electronic topological transition in Sb_2S_3. J Phys Condens Matter. 2015; 28: 015602.
32. Escorcia-García J, Domínguez-Díaz M, Hernández-Granados A, Martínez H. Antimony sulfide thin films obtained by chemical bath deposition using tartaric acid as complexing agent. MRS Adv. 2018; 3: 3307-3313.
33. Raghni ME, Bonnet B, Hafid ML, Olivier-Fourcade J, Jumas JC. Raman spectroscopic study of the ternary system Sb_2S_3-As_2S_3-Tl_2S. J Alloys Compd. 1997; 260: 7-11.
34. Tauc J, Grigorovici R, Vancu A. Optical properties and electronic structure of amorphous germanium. Phys Status Solidi B. 1966; 15: 627-637.
35. Hassanien AS, Sharma I. Band-gap engineering, conduction and valence band positions of thermally evaporated amorphous $Ge_{15-x}Sb_xSe_{50}Te_{35}$ thin films: Influences of Sb upon some optical characterizations and physical parameters. J Alloys Compd. 2019; 798: 750-763.
36. Naik R, Jain A, Ganesan R, Sangunni KS. Compositional dependence optical properties study of $As_{40}Se_{60-x}Sb_x$ thin films. Thin Solid Films. 2012; 520: 2510-2513.
37. Naik R, Sahoo PP, Sripan C, Ganesan R. Laser induced Bi diffusion in $As_{40}S_{60}$ thin films and the optical properties change probed by FTIR and XPS. Opt Mater. 2016; 62: 211-218.
38. Hassanien AS, El Radaf IM. Effectiveness of Sn-addition on optical properties and physicochemical parameters of $Sn_xSb_{2-x}Se_3$ thin films. Mater Chem Phys. 2023; 303: 127827.
39. Hassanien AS, Sharma I. Synthesis, analysis, and characterization of structural and optical properties of thermally evaporated chalcogenide a-Cu-Zn-Ge-Se thin films. Mater Chem Phys. 2024; 311: 128524.
40. El Radaf IM, Al-Zahrani HY, Hassanien AS. Novel synthesis, structural, linear and nonlinear optical properties of p-type kesterite nanosized Cu_2MnGeS_4 thin films. J Mater Sci Mater Electron. 2020; 31: 8336-8348.
41. Yang JW, Ji SG, Jeong CS, Kim J, Kwon HR, Lee TH, et al. High-efficiency unbiased water splitting with photoanodes harnessing polycarbazole hole transport layers. Energy Environ Sci. 2024; 17: 2541-2553.